Measurement of Exclusive ρ^0 Meson Photoproduction at HERA

H1 Collaboration

Abstract

Exclusive photoproduction of ρ^0 vector mesons is studied using the H1 detector at HERA. A sample of about 700000 decays $\rho^0 \rightarrow \pi^+\pi^-$ was collected in the years 2006-2007, using the H1 Fast Track Trigger. It corresponds to an integrated luminosity of 1.3 pb^{-1}. The sample is used to study cross-sections as a function of the invariant mass $m_{\pi^+\pi^-}$ of the decay pions, the photon-proton collision energy $W_{\gamma p}$ and the momentum transfer at the proton vertex t. The phase-space restrictions are $0.5 < m_{\pi^+\pi^-} < 1.3$ GeV, $20 < W_{\gamma p} < 80$ GeV and $|t| < 1.5$ GeV^2. Reactions where the proton stays intact are statistically separated from those where the proton dissociates to a low-mass hadronic system. The observed cross-section dependencies are parameterized using fits and are compared to expectations from phenomenological models.

1 Introduction

This document is a brief description of the measurement of the elastic and proton-dissociative ρ^0 photoproduction cross-section as a function of the center-of-mass energy $W_{\gamma p}$. The analysis uses H1 data collected from the high energy electron-proton collisions at HERA in 2006 and 2007. The sample of photoproduced $\pi^+\pi^-$ events used for the analysis is described in Section 2. The MC samples used to model the data are introduced in Section 3. The ρ^0 cross-sections are extracted from the $\pi^+\pi^-$ data in two steps: first the $\pi^+\pi^-$ distributions are unfolded to particle level, then the ρ^0 contribution to the $\pi^+\pi^-$ cross-section is extracted using an extended Söding model. Both steps are described in Section 4. The results are presented in Section 5.

2 Data-Set

The analysis is based on a sample of exclusive $\pi^+\pi^-$ events collected with the H1 detector in 2006 and 2007. A detailed description of the H1 detector can be found elsewhere [1]. For the dataset only events where protons at an energy of 920 GeV were collided with 27.6 GeV positrons[1] are considered. Given the varying trigger pre-scales the sample corresponds to an integrated luminosity of $\mathcal{L}_{int} = 1.3$ pb^{-1}. The selection of the dataset is outlined in the following.

The pions from ρ^0 photoproduction are expected to be centrally produced with low transverse momenta $p_T \lesssim 1$ GeV. In the photoproduction regime, the electron leaves the detector undetected, as in most cases also does the strongly forward[2] scattered proton. To trigger such events a mostly track-based, dedicated ρ^0 trigger was used. Track information within the 2.3 μs decision time of the H1 level-1 trigger was available through the Fast Track Trigger (FTT). The FTT used pattern recognition and associative memory to identify predefined tracks in the hit-patterns produced by charged particles in a subset of the central jet chamber (CJC) wires. For a positive trigger decision, at least two FTT tracks above a transverse momentum threshold of 160 MeV and at most three tracks above a threshold of 100 MeV had to be reconstructed . The sum of the charges of these tracks must not exceed $\pm 1e$. In addition, trigger information from the Central Inner Proportional Chamber (CIP) was used to ensure a low multiplicity interaction within the nominal interaction region. And vetoes on the inner, forward part of the Liquid Argon (LAr) calorimeter, and a scintillator wall in forward direction were applied to suppress interactions in which the scattered proton dissociates into a system with high mass.

In order to select a pure sample of $\pi^+\pi^-$ photoproduction events a set of off-line selection cuts is applied on top of the trigger requirements:

- The reconstructed primary vertex is required to be within 25 cm of the nominal interaction point along the beam axis.

---

[1]In the following the term "electron" is indistinctly used to refer to both electrons and positrons.

[2]A right handed cartesian coordinate system is used with the origin at the nominal primary ep interaction vertex. The proton beam direction defines the z axis. The polar angles θ and transverse momenta p_T of all particles are defined with respect to this axis. The azimuthal angle ϕ defines the particle direction in the transverse plane. The pseudorapidity is defined as $\eta = -\ln \tan \frac{\theta}{2}$.

- No scattered electron candidate is reconstructed in neither the LAr nor SpaCal calorimeter.

- Exactly two primary-vertex fitted, central tracks of good quality are reconstructed. They are required to have opposite charge and be within the CJC acceptance defined as $p_T > 160$ MeV and $20° < \theta < 160°$. Low momentum kaons, protons and deuterons are suppressed using the measured energy loss of the tracks in the CJC.

- There are no LAr or SpaCal clusters with energies above a noise threshold 400 MeV and 200 MeV, respectively, that cannot be associated with one of the tracks. A cluster is considered associated to a track if it lies within a cylinder of a radius of 30 cm along the direction of the particle's momentum at calorimeter entry.

From the four-momenta of the two reconstructed pion candidates, the momentum transfer at the proton vertex t and the photon-proton center-of-mass energy $W_{\gamma p}$ can be approximately reconstructed:

$$t \simeq -p_{T,\pi^+\pi^-}^2, \quad \text{and} \tag{1}$$

$$W_{\gamma p} \simeq \sqrt{2E_p(E_p - p_{z,\pi^+\pi^-})}. \tag{2}$$

E_p here denotes the proton-beam energy and $p_{T,\pi^+\pi^-}$ and $p_{z,\pi^+\pi^-}$ are the transverse and longitudinal four-momentum component of the $\pi^+\pi^-$ system. The two relations only exactly hold for photoproduction with photon-virtuality $Q^2 = 0$; however, the electron veto limited by the SpaCal acceptance only guarantees $Q^2 \lesssim 2.5$ GeV.

The experimental phasespace considered in this analysis is defined by cuts on $W_{\gamma p}$, t, and the invariant $\pi^+\pi^-$ mass $m_{\pi^+\pi^-}$:

$$
\begin{array}{rcll}
15 & < & W_{\gamma p}[\text{GeV}] & < \quad 100, \\
0 & < & p_{T,\pi^+\pi^-}^2[\text{GeV}^2] & < \quad\quad 2, \quad \text{and} \\
0.3 & < & m_{\pi^+\pi^-}[\text{GeV}] & < \quad 1.5.
\end{array}
$$

The data is modelled using a set of MC samples for signal and background processes; see Section 3. Another background contribution due to beam-restgas and beam-machine interactions is estimated using events from pilot-bunch collisions where a proton or electron bunch is purposefully collided with a gap in the oncoming bunch-structure. The signal purity of the data-sample is about 94%. The dominant background components are from:

- higher mass ρ' resonances, which decay into multiple charged or neutral pions, some of which escape detection,

- $\omega \to \pi^+\pi^-\pi^0$ decays where the low-momentum π^0 escapes detection

- beam-restgas and beam-machine interaction events producing low-mass particles

- ϕ decays into kaon-pairs that are mis-identified as pions, and

2

- γ-dissociation events where hadronic photon system decays into a multitude of low-mass particles in the very backward direction.

To study and constrain these backgrounds, some of the selection cuts defined above are inverted or modified to define control regions enriched in one of the dominant background components.

- A ϕ control region is defined by identifying the two tracks as kaons via their measured energy loss in the central tracker and requiring the invariant mass reconstructed under the kaon hypothesis to be within 15 MeV of the $\phi(1020)$ mass. The ϕ purity achieved in this region is $\sim 90\%$.

- Events with energy clusters in the LAr and optionally a moderate energy deposit in the SpaCal constitute an ω ($\sim 48\%$ purity) or ρ' ($\sim 71\%$ purity) control region depending whether the invariant mass of the tracks and all unassociated clusters is below or above 600 MeV.

- Events with an unassociated energy deposit in the SpaCal between 2 and 10 GeV constitue a control region for photon-dissociative events ($\sim 52\%$ purity).

In Figure 2 the distribution of the selected number of events is shown as a function of the invariant $\pi^+\pi^-$ mass and compared to the MC model. The ρ^0 resonance at a mass of ~ 770 MeV clearly dominates the sample. Smaller contributions to $\pi^+\pi^-$ production are implicitly modelled by the ρ^0 MC, as well, which is tuned to better describe the data; see Section 3. Most events originate from elastic scattering of the proton, but the sample still obtains a significant contribution from proton-dissociation. Various wrongly reconstructed background events contaminate the sample at percent level. At low mass, a broad peak is attributed to $\omega(782)$ production, much wider backgrounds are attributed to $\rho(1450)$, $\rho(1700)$, γ-dissociation and beam-gas interactions. Contamination from ϕ events is all but negligible. Correspondingly to the mass distribution in Figure 3 the $W_{\gamma p}$ and $p^2_{T,\pi^+\pi^-}$ distributions in the signal region are shown.

2.1 Tagging p-Dissociative Events

A fraction of the selected data-sample is from interactions where the scattered proton decays into a system Y of several particles with a combined invariant mass M_Y larger than the mass of the proton m_p. The aforementioned selection cuts on the unassociated energy deposits limit the system to approximately $M_Y \lesssim 10$ GeV. While the elastically scattered proton leaves the detector undetected through the beam-pipe, particles of Y can obtain sufficient transverse momentum to be detected by one of several detectors in the forward region. Information from the H1 forward muon detectors (FMD), the plug calorimeter and the Forward Tagging Station (FMD) 28m down the beam-pipe is used to tag these events. In order to improve the tagging efficiency and reduce the mis-tag rate, the binary "tag/no-tag" information from the three detectors is combined into three tagging categories: a zero tag, single tag and multi-tag category. By splitting the dataset into these categories the elastic events can be well separated from the proton-dissociative events: The zero tag category is dominated by $\sim 90\%$ elastic events, int0 the single tag category this fraction is reduced to 52%, and the multi-tag category consists of 92% proton-dissociative events.

3 Monte Carlo Modelling

The data are modelled using MC samples for elastic and proton-dissociative ρ^0, $\omega(782)$, $\phi(1020)$, $\rho(1450)$, $\rho(1700)$ production, as well as for elastic photon-dissociation. The samples are all generated using the DiffVM event generator [2] that models vector meson production on the principles of equivalent photon approximation [3], the vector meson dominance model [15–19], and pomeron exchange [20–22]. For the vector mesons the following decay channels are considered:

- For the ρ^0, ω and ϕ sample all observed decay channels are modelled with their respective measured branching fractions if they account for at least 1% of the mesons' decays.

- The various $\rho(1450)$, and $\rho(1700)$ decay modes have not been measured in detail. The estimated decay channels assumed in the MC are $\rho^{\pm}\pi^{\mp}\pi^0$ and $\rho^0\pi\pi$ at a branching fraction of 30% per charge combination, $2\pi^+2\pi^-$ at 6%, $\pi^+\pi^-2\pi^0$ at 2%, and $\pi^+\pi^-$ at 2%.

- The fragmentation process in the photon-dissociative MC is modelled via JETSET [10].

- All events with a $\pi^+\pi^-$ final state are removed from the background samples and treated as signal. Contributions from $\omega(782) \rightarrow \pi^+\pi^-$ and γ-dissociation $\rightarrow \pi^+\pi^-$ are explicitly included in the ρ^0 by reweighing the $m_{\pi^+\pi^-}$ lineshape. Contributions from the $\rho(1450)$ and $\rho(1700)$ samples are neglected.

Proton dissociation is modelled by DiffVM assuming the following dependence of the cross-section on the mass of the dissociated system:

$$\frac{\mathrm{d}\sigma^{\gamma}p}{dM_Y^2} = \frac{f(M_Y)}{(M_Y^2)^{1+\epsilon_Y}}. \tag{3}$$

Here, $\epsilon_Y = 0.0808 \pm 0.01$ and $f(M_Y)$ is a phenomenological function that is fitted to the experimental data [23,24] to parametrize the low-mass resonance structure in the region $m_p < M_Y < 1.9$ GeV. For $M_Y > 1.9$ GeV $f(M_Y)$ becomes constant. In the low mass region the dissociative system is treated as an N^* resonance and decays are modelled according to measured branching fractions [25]. For higher masses the decay is modelled as a Lund fragmentation process as implemented in.

To a large extend DiffVM provides only phenomenological kinematic spectra. In order to achieve a better agreement between data and the MC model, all DiffVM samples are reweighed on generator level in t and $W_{\gamma p}$. The ρ^0 samples are also reweighed in $m_{\pi^+\pi^-}$ in order to account for contributions to the $\pi^+\pi^-$ spectrum not coming from the ρ^0 resonance.

The background MCs are reweighed to the following $W_{\gamma p}$ and t dependence of the photo-production cross-section:

$$\frac{\mathrm{d}\sigma^{\gamma p}}{\mathrm{d}t}(W_{\gamma p}) = \left(\frac{W_{\gamma p}}{90 \text{ GeV}}\right)^{4(\alpha-1)} \exp(b\,t), \tag{4}$$

where α and b are reweighing parameters to be chosen. For the elastic ω, ϕ, ρ, ρ, and γ-dissociation samples α is set to $\alpha^{\text{elas}} = 1.06 \pm 0.03$, and the corresponding proton-dissociation

samples to $\alpha^{p\text{-diss}} = 1 \pm 0.03$. For the elastic ω and ϕ samples $b_\omega^{\text{elas}} = 10 \pm 1.8$ GeV^{-1} and $b_\phi^{\text{elas}} = 6.3 \pm 1$ GeV^{-1} are taken from measurements by [26] and [27], respectively. For the elastic $\rho(1450)$, and $\rho(1700)$ and the γ-dissociation samples the b^{elas}-parameters are tuned using the dataset at hand and set to $b_{\rho'} = b_{\gamma-\text{diss}} = 5.2 \pm 1$. For the proton-dissociative ϕ sample $b_\phi^{p\text{-dis}} = 2.1 \pm 0.9$ was measured by [27], as well. All other proton-dissociative $b^{p\text{-dis]}}$-parameters are set to half the corresponding elastic values.

The $\rho(1450)$ and $\rho(1700)$ samples can not be well distinguished experimentally in this analysis. They are thus combined at a $(2 \pm 1) : 1$ ratio and treated as a single MC sample. Furthermore, for all background samples the elastic contributions can not be well distinguished from the proton-dissociative contributions and are also combined. From the template fit described below, an estimated fraction of $36 \pm 1\%$ of the reconstructed events are proton-dissociative which is assumed for the combination.

A deviation from pure exponential t-dependence of the cross-section is needed to describe the $\pi^+\pi^-$ sample. The ρ^0 MCs are thus reweighed to the cross-section:

$$\frac{\mathrm{d}\sigma^{\gamma p}}{\mathrm{d}t}(W_{\gamma p}) = \left(\frac{W_{\gamma p}}{90 \text{ GeV}}\right)^{4(\alpha_0+\alpha_1\, t-1)} \exp\left(a\ln(1 - b\,t/a)\right). \tag{5}$$

The chosen parametrization for the t dependence smoothly interpolates between an exponential behaviour $\mathrm{d}\sigma^{\gamma p}/\mathrm{d}t \propto \exp\left(b\,t + b^2\,t^2/2a\right)$ at low $|t|$ and a power law $\mathrm{d}\sigma^{\gamma p}/\mathrm{d}t \propto |t|^{-a}$ at large $|t|$.

Furthermore, the reproduce the full $\pi^+\pi^-$ mass spectrum with contributions from the ω resonance and non-resonant production the samples are reweighed in $m_{\pi^+\pi^-}$ to the extended Söding model that is defined in Equation (10) in Section 4. All mass parameters are assumed to be the same for the elastic and proton-dissociative sample and most are assumed to be independent of $W_{\gamma p}$ and t. Only for the parameters $f_{nr} = f_{nr}(t)$ and $\Lambda_{nr} = \Lambda_{nr}(t)$ a t-dependence is assumed:

$$f_{nr}(t) = f_{nr}^0 \exp\left(f_{nr}^1\, t\right) \tag{6}$$

$$\Lambda_{nr}(t) = \sqrt{\Lambda_{nr,0}^2 - t} \tag{7}$$

All reweighing parameters for the ρ^0 samples are tuned to the data-set at hand to achieve a good description within uncertainties. The tuning is done via a template fit of the MC model to three dimensional histograms of the detected number of events in $W_{\gamma p}$, $p_{T,\pi^+\pi^-}^2$ and $m_{\pi^+\pi^-}$ in the three tagging and all four background regions. The number of bins is adapted in each region to the number of events in that region. In addition to the reweighing parameters the normalizations of all samples is determined in the fit. However, the relative fraction of proton-dissociative background events is not well constrained by the fit and is thus fixed to the fitted fraction for the ρ^0 sample. The optimized ρ^0 parameters are summarized in Table 1.

All generated events are passed through the full GEANT [30] based simulation of the H1 apparatus and are reconstructed using the same program chain as for the data. Trigger scaling factors are applied to correct differences in the trigger performance between data and simulation. They are obtained from $\pi^+\pi^-$ sample from deep-inelastic scattering events, that can be triggered track-independently by the scattered electron.

Table 1: ρ^0 MC reweighing parameters.

mass parameter		value	$W_{\gamma p}$-t parameter		value
m_ρ	[GeV]	0.7707 ± 0.0003	α_0^{elas}		1.0606 ± 0.002
$\Gamma_{\rho,0}$	[GeV]	0.1458 ± 0.0006	α_1^{elas}	[GeV^{-2}]	0.2412 ± 0.015
f_ω		0.031 ± 0.002	a^{elas}		14.6 ± 1
ϕ_ω		1.72 ± 0.06	b^{elas}	[GeV^{-2}]	11.47 ± 0.09
m_ω		PDG value	$\alpha_0^{p\text{-dis}}$		0.9567 ± 0.006
$\Gamma_{\omega,0}$		PDG value	$\alpha_1^{p\text{-dis}}$	[GeV^{-2}]	0.0455 ± 0.013
f_{nr}^0		0.90 ± 0.01	$a^{p\text{-dis}}$		6.1 ± 0.5
f_{nr}^1		2.52 ± 0.05	$b^{p\text{-dis}}$	[GeV^{-2}]	6.16 ± 0.12
ϕ_{nr}		3.01 ± 0.01			
δ_{nr}		0.7 ± 0.1			
$\Lambda_{nr,0}$	[GeV]	0.3 ± 0.01			

4 Determination of the ρ^0 Photoproduction Cross-Section

The detector level data distributions are unfolded to extract differential cross-section distributions on truth particle level. This means that the simulated detector response from the MC samples is used to correct the detected number of events for the limited detector acceptance, the reconstruction efficiency and resolution, and to separate elastic from proton-dissociative events. The fiducial phasespace for the measured cross-section is chosen to be slightly smaller than the experimental phasespace. This allows to properly account for migrations of events in and out of the phasespace due to detector resolution effects. The fiducial phasespace is defined in Table 2.

The unfolding is done by means of a binned, regularized template fit, which is described in the following. In sections thereafter the differential $\pi^+\pi^-$ photoproduction cross-section is defined and the extraction of the ρ^0 contribution is explained.

4.1 Unfolding With TUnfold

This analysis uses the TUnfold [8] package to unfold binned detector level distributions. Efficiency and migration effects are modelled by a migration matrix A that is obtained from MC

Table 2: Definition of the fiducial phasespace. The cuts on $W_{\gamma p}$, t, and $m_{\pi^+\pi^-}$ are applied on truth and detector level, whereas explicit cuts on Q^2 and M_Y are only possible on truth level. The kinematic region of M_Y is used to separately define elastic and proton-dissociative cross-sections.

20	$<$	$W_{\gamma p}$	[GeV]	$<$	80,
0	$<$	t	[GeV^2]	$<$	1.5
0.4	$<$	$m_{\pi^+\pi^-}$	[GeV]	$<$	1.2
0	$<$	Q^2	[GeV^2]	$<$	0.1

elastic	proton-dissociative				
$M_Y = m_p$	m_p	$<$	M_Y	[GeV]	$<$ 10

simulation. Let the vectors $\vec{x}_{\text{true}}^{MC}$ and $\vec{y}_{\text{rec}}^{MC}$ represent the true and reconstructed MC distributions, then each matrix element A_{ij} gives the probability that an event originating from bin j of $\vec{x}_{\text{true}}^{MC}$ is reconstructed in bin i of $\vec{y}_{\text{rec}}^{MC}$, which can be written as a matrix equation

$$\vec{y}_{\text{rec}}^{MC} = \boldsymbol{A} \cdot \vec{x}_{\text{true}}^{MC}. \tag{8}$$

To estimate the number of true events $\hat{\vec{x}}$ corresponding to the observed reconstructed data distribution $\vec{y}_{\text{rec}}^{\text{data}}$ a χ^2-function $\chi^2(\vec{x}|\vec{y}_{\text{rec}}^{\text{data}}, \boldsymbol{A})$ is defined and minimized by varying $\vec{x}$. In order to suppress correlated statistical fluctuations in the unfolded distribution $\hat{\vec{x}}$ the χ^2-function is extended by regularization constraints on the normalization and the smoothness of the second derivative of $\hat{\vec{x}}$. The regularization strength is chosen such that the average global correlation between the bins of $\hat{\vec{x}}$ is minimized.
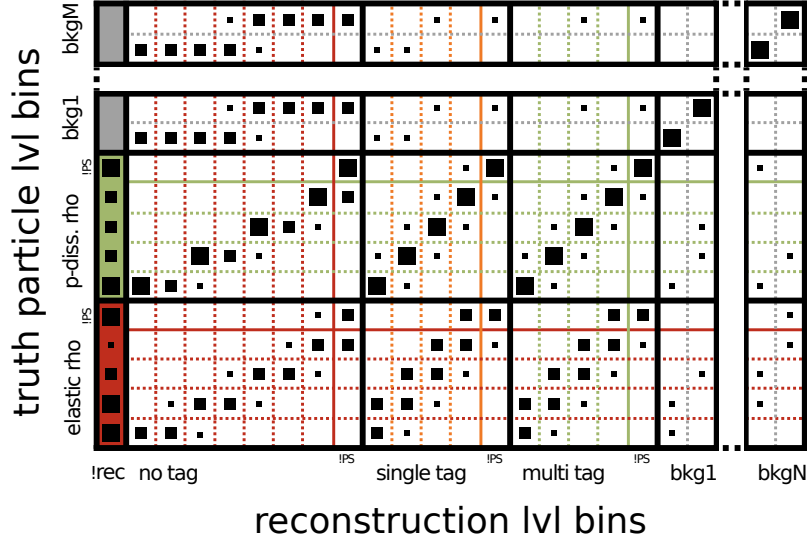
Figure 1: Response matrix schematic.

The structure of the response matrix used in this analysis is illustrated in Figure 1, where the x-axis corresponds to the reconstructed and the y-axis to the truth distribution. Along the x-axis the response matrices from the different MC sources are stacked, which allows to separate respective contributions to the measured spectrum. Sub-matrices from the elastic and proton-dissociative signal MC and from the four background MCs from ω, ϕ, $\rho(1450 + 1700)$, γ-dissociation are considered. For the latter the truth variables to be unfolded can not always be well defined. Instead, these sub-matrices track how the *reconstructed* background MC events from the different background sources contribute to the, differently defined, reconstructed distribution. This results in a subtraction of background events where the background normalization in each truth distribution bin is determined in the unfolding. Along the x-axis, the reconstructed distribution is split into multiple control regions: the three forward tagging regions to constrain contributions from elastic and proton-dissociative events plus four background control regions to constrain the contributions from the respective background processes.

4.2 $\pi^+\pi^-$ Photoproduction Cross-Section

The differential $\pi^+\pi^-$ photoproduction cross-section is defined as:

$$\frac{\mathrm{d}^2\sigma^{\gamma p \to \pi^+\pi^- X}(t, W_{\gamma p}, m_{\pi^+\pi^-})}{\mathrm{d}t\mathrm{d}m_{\pi^+\pi^-}} = \frac{N^X_{\text{unfolded}}}{\mathcal{L}_{\text{int}}\Delta t\,\Delta m_{\pi^+\pi^-}\,\Phi_{\gamma/e}(W_{\gamma p})}. \tag{9}$$

N^X_{unfolded} is the number of unfolded events in a given bin, $\mathcal{L}_{int}$ the integrated luminosity of the considered dataset, and Δt, and $\Delta m_{\pi^+\pi^-}$ are the bin-widths in t, and $m_{\pi^+\pi^-}$, respectively. The measured ep cross-section is normalized by a photon flux factor $\Phi_{\gamma/e}(W_{\gamma p})$ to transformed it into a photoproduction cross-section. For this analysis $\Phi_{\gamma/e}(W_{\gamma p})$ is calculated using the Weizsäcker-Williams formula [11–14] integrated over the considered range $0 \le Q^2 < 0.1~\mathrm{GeV}^2$.

4.3 Mass-Dependence and Extraction of the ρ^0 Contribution

While the $\pi^+\pi^-$ cross-section is dominated in the considered mass range by the ρ^0 resonance, it obtains significant contributions from the $\omega(782)$ resonance, as well as non-resonant $\pi^+\pi^-$ production. At higher $m_{\pi^+\pi^-}$ values, further resonances have been observed. In the mass range $0.4 < m_{\pi^+\pi^-} < 1.3$ GeV an extended Söding model [28] is used to describe the complete $m_{\pi^+\pi^-}$ spectrum:

$$\frac{d\sigma}{dm_{\pi^+\pi^-}}(m_{\pi^+\pi^-}) = \frac{N}{(1 + f_\omega + f_{nr})^2} \tag{10}$$

$$\cdot \left[\mathcal{RBW}_\rho(m_{\pi^+\pi^-}) + f_\omega e^{i\phi_\omega}\mathcal{RBW}_\omega(m_{\pi^+\pi^-}) + f_{nr}e^{i\phi_{nr}}\frac{B_{nr}(m_{\pi^+\pi^-})}{B_{nr}(m_\rho)}\right]^2,$$

where a ρ^0 and ω contribution are each parametrized by a relativistic Breit-Wigner amplitude [29]

$$\mathcal{RBW}_{\mathrm{VM}}(m_{\pi^+\pi^-}) = \frac{\sqrt{m_{\pi^+\pi^-}m_{\mathrm{VM}}\Gamma(m_{\pi^+\pi^-})}}{m_{\pi\pi}^2 - m_{\mathrm{VM}}^2 + i\,m_{\mathrm{VM}}\Gamma(m_{\pi^+\pi^-})} \tag{11}$$

with mass-dependent width

$$\Gamma(m_{\pi^+\pi^-}) = \Gamma_{\mathrm{VM},0}\left(\frac{m_{\pi\pi}^2 - 4m_\pi^2}{m_{\mathrm{VM}}^2 - 4m_\pi^2}\right)^{\frac{3}{2}}\frac{m_{\mathrm{VM}}}{m_{\pi^+\pi^-}}. \tag{12}$$

A non-resonant contribution is parametrized by

$$B_{nr} = \left(\frac{m_{\pi^+\pi^-} - 2m_\pi}{(m_{\pi^+\pi^-} - 2m_\pi)^2 + \Lambda_{nr}^2}\right)^{\delta_{nr}}. \tag{13}$$

In these equations N is a normalization parameter, m_{VM} and $\Gamma_{\mathrm{VM},0}$ denote the vector mesons' mass and width, and Λ_{nr} and δ_{nr} are phenomenological parameters shaping the non-resonant background, respectively. f_ω and f_{nr} are the relative normalizations of the ω and non-resonant contribution and, through ϕ_ω and ϕ_{nr}, global phase-differences between the two vector mesons,

as well as between the ρ^0 and the non-resonant component are explicitly allowed. The parametrization of the non-resonant contribution was chosen because it allows to describe the $m_{\pi^+\pi^-}$ spectrum well, including it's strong t-dependence. The model can be extended to higher masses by including a third Breit-Wigner resonance analogously to the ω contribution that will be generically referred to as a ρ' contribution.

In order to extract the ρ^0 contributions to the $\pi^+\pi^-$ cross-section, the unfolded mass distributions are fitted using Equation (10). The ρ^0 contribution is then defined by the integral:

$$\sigma(ep \to \rho^0 p) = \int_{2m_\pi}^{m_\rho+5\Gamma_\rho} \left| \mathcal{RBW}_\rho(m_{\pi^+\pi^-}) \right|^2 \mathrm{d}m_{\pi^+\pi^-}. \tag{14}$$

The integration boundaries are always defined by the PDG values for m_π, m_ρ, and Γ_ρ ("Photo-produced") [25] such that $m_\rho + 5\Gamma_\rho \simeq 1.53$ GeV, whereas in $\mathcal{RBW}_\rho$ the fitted mass and width parameters are used. An uncertainty on the ρ^0 cross-section is calculated by propagating the correlated fit parameter uncertainties through the integral. The non-resonant contribution to the cross-section in that mass range is calculated analogously.

To extract kinematic dependencies of the ρ^0 cross-section, the $\pi^+\pi^-$ mass distribution is fitted in $W_{\gamma p}$ bins. Not all parameters of the extended Söding model can be well constrained independently in all individual bins or even for the elastic and proton-dissociative part of the cross-section. That is why for the parallel fits further model assumptions on the parameter dependences on the mass of the proton final state M_Y, $W_{\gamma p}$ and t are made. They are summarized in Table 3. In particular, the available $m_{\pi^+\pi^-}$ resolution is not sufficient to resolve the with of the $\omega(782)$ resonance, which is thus always fixed to the PDG value $\Gamma_{=omega,0} = 8.5$ MeV. The mass of the $\omega(782)$ can be fitted in the one-dimensional mass distribution only, in is fixed for the parallel fits in $W_{\gamma p}$ to the value obtained there to allow for the possibility of absolute systematic shifts in the mass scale that have not been studied yet.

4.4 Parallel Fits and χ^2 Definition

The differential cross-sections are parametrized and fitted with the goal to extract more fundamental parameters, such as the ρ^0 contribution. Only one-dimensional parametrizations are used, however for multi-dimensional cross-section dependences the one-dimensional distributions are always fitted in parallel. For example the $m_{\pi^+\pi^-}$ dependence of the cross-section is fitted in parallel for the elastic and proton-dissociative distribution, for the one-dimensional case and in all $W_{\gamma p}$ bins for the two-dimensional cross-section. This allows to take the full correlations between all bins into consideration and also to better constrain some fit parameters that are shared across all distributions. The fits are performed by optimizing the fit parameters $\vec{\theta}$ to minimize the χ^2

$$\chi^2(\vec{\theta}) = \sum_{i_{\text{distr.}}=0}^{n_{\text{distr.}}} \sum_{j_{\text{distr.}}=0}^{n_{\text{distr.}}} \left[\vec{\sigma}_{i_{\text{distr.}}}(m) - \vec{\mathcal{F}}(m,\vec{\theta}) \right]^T (\boldsymbol{U}_\sigma^{\text{stat}})^{-1}_{i_{\text{distr.}},j_{\text{distr.}}} \left[\vec{\sigma}_{j_{\text{distr.}}}(m) - \vec{\mathcal{F}}(m,\vec{\theta}) \right] \tag{15}$$

$\vec{\sigma}$ is the one-dimensional cross-section distribution along variable m, $\boldsymbol{U}_\sigma^{\text{stat}}$ the statistical covariance matrix and $\vec{\mathcal{F}}(m,\vec{\theta})$ the bin-averaged fit function in each bin of the distribution. If the

parameter	M_Y-dependent	$W_{\gamma p}$-dependent
m_{ρ^0}	✗	✗
$\Gamma_{\rho,0}$	✗	✗
f_ω	✓	✗
ϕ_ω	✓	✗
m_ω	✗	✗
$\Gamma_{\omega,0}$	✗	✗
f_{nr}	✓	✓
ϕ_{nr}	✓	✗
δ_{nr}	✗	✗
Λ_{nr}	✓	✗
$f_{\rho'}$	✓	
$\phi_{\rho'}$	✓	
$m_{\rho'}$	✗	
$\Gamma_{\rho',0}$	✗	

Table 3: Multi-dimensional parameter dependences of the extended Söding model parameters defined in Equation (10). The labels ✓ and ✗ indicate whether a parameter is assumed to depend on M_Y or $W_{\gamma p}$, and thus set as a single parameter across all distributions in the parallel fits. Empty cells indicate that a parameter is not used in the given kind of parallel fit.

differential cross-section is parametrized by $f(m, \vec{\theta})$, $\mathcal{F}_i$ in a given bin $[m_i - \Delta_i/2, m_i + \Delta_i/2]$ is defined as

$$\mathcal{F}_i = \frac{1}{\Delta_i} \int_{m_i - \Delta_i/2}^{m_i + \Delta_i/2} f(m, \vec{\theta}) \mathrm{d}m. \tag{16}$$

4.5 Systematic Uncertainties

Several sources of systematic uncertainties are considered:

- The MC modelling parameters defined in Section 3 are varied; as are the Q^2 dependence of both ρ^0 MCs, the M_Y dependence of the proton-dissociative ρ^0 MC and the relative fraction of proton-dissociative background events.

- The LAr and SpaCal energy scales are independently varied by $\pm 10\%$, their noise levels are changed by by $\pm 50\%$ and a modification of the cluster association radius of $\pm 30\%$ is considered.

- The tagging efficiency of the Plug, FTS and FMD tags for elastic and proton-dissociative MCs is independently varied by $\pm 10\%$ (relative).

- A statistical uncertainty on the trigger scaling factors as as well as an uncertainty due to the transport of the DIS correction factors to photoproduction kinematics is considered.

- A $\pm 20\%$ uncertainty is applied on the modelling of the track p_T resolution.

- A normalization uncertainty from the luminosity measurement of 2.7% is considered, as well as 2% track reconstruction uncertainty (1% per track).

For each variation almost the full analysis chain is repeated with three noticeable exceptions:

a) In the unfolding always the same regularization strength τ is used, which is obtained from minimizing the nominal average global correlation.

b) All variations are symmetrized around the nominal distribution after the unfolding step, in particular only the symmetrized variations are considered in the cross-section fits. For one-sided variations (e.g. from the trigger correction) the full uncertainty is applied in both direction.

c) For the cross-section fits always the nominal statistical uncertainties are used in the χ^2 definition.

5 Results

Differential elastic and proton-dissociative $\pi^+\pi^-$ photoproduction cross-sections are measured in the phase-space defined in Table 2. The one-dimensional cross-section as a function of $m_{\pi^+\pi^-}$ is used to illustrate the structure of the $\pi^+\pi^-$ mass spectrum and to interpret it using the extended Söding model defined in Equation (10). The model is then applied to the two-dimensional $\pi^+\pi^-$ cross-section as a function of $m_{\pi^+\pi^-}$ and $W_{\gamma p}$ and used to extract the energy dependence of the ρ^0 cross-section.

5.1 $\pi^+\pi^-$ Mass Spectrum

The differential cross-section $\mathrm{d}\sigma(\gamma p \to \pi^+\pi^- X)/\mathrm{d}m_{\pi^+\pi^-}$ is shown in Figure 4 as function of $m_{\pi^+\pi^-}$ for both elastic and proton-dissociative scattering. The distributions are obtained by unfolding the one-dimensional $m_{\pi^+\pi^-}$ distribution. A simultaneous fit of the parametrization given in Equation (10) to both distributions is performed to determine the model parameters. The fit functions are shown in the figure together with the ρ^0, ω and non-resonant contributions and the combination of all interference terms. The fit illustrates that while the total cross-section is dominated by ρ^0 production, the line-shape of the $m_{\pi^+\pi^-}$ distribution is strongly distorted by the other contributions because of strong interference terms. These result in a steep edge right above the ρ^0 mass peak and a strong skewing of the ρ^0 resonance towards smaller mass values.

The skewing of the ρ^0 peak is significantly weaker in the proton-dissociative cross-section. This can be seen model independent in Figure 5 where the elastic and proton-dissociative cross-sections are directly compared as a function of $m_{\pi^+\pi^-}$.

The fiducial elastic and proton-dissociative $\pi^+\pi^-$ cross-section obtained from unfolding the mass distribution are given in Table 4.

11

While this analysis focuses on the ρ^0 resonance, further resonances with a larger mass have been observed in the $\pi^+\pi^-$ spectrum for example by ZEUS [9] in $\pi^+\pi^-$ electroproduction events. Also in the data-set at hand such a resonance at around $m_{\pi^+\pi^-} = 1.6$ GeV can be observed as is shown in Figure 6 where the upper limit on $m_{\pi^+\pi^-}$ for the cross-section $\mathrm{d}\sigma(\gamma p \to \pi^+\pi^- p)/\mathrm{d}m_{\pi^+\pi^-}$ is increased up to 2.2 GeV. The mass spectrum is again fitted using the extended Söding model with one additional Breit-Wigner contribution to account for this high mass resonance. The fit functions are shown together with the cross-sections including a set of individual contributions to the full model.

5.2 Energy Dependence of the ρ^0 Cross-Section

In order to measure the energy dependence of the ρ^0 cross-section, the $\pi^+\pi^-$ cross-section $\mathrm{d}\sigma(\gamma p \to \pi^+\pi^- X)/\mathrm{d}m_{\pi^+\pi^-}$ is measured as a function of $m_{\pi^+\pi^-}$ and $W_{\gamma p}$. It is obtained by unfolding the two-dimensional $m_{\pi^+\pi^-} \otimes W_{\gamma p}$ distributions and shown in Figures 6 and 7 as a function of $m_{\pi^+\pi^-}$ in the $W_{\gamma p}$ bins for elastic and proton-dissociative events. The distributions are fitted in parallel using the extended Söding model with the assumptions on the parameters' $W_{\gamma p}$ dependence that are summarized in Table 3. The fit functions are shown together with the distributions, including individual contributions to the full model. Following the procedure outlined in Section 4.3 the energy dependence of the ρ^0 and non-resonant contribution can be extracted by integrating out the mass dependence of the corresponding contributions to the fit. The results are shown in Figure 8. For both the full $\pi^+\pi^-$ cross-section, as well as the ρ^0 and non-resonant contribution the elastic cross-section slightly rises with energy. For the proton-dissociative cross-section on the other hand, no significant energy dependence can be observed.

The energy dependence of the cross-sections $\sigma(\gamma p \to \rho^0 X)$ is put into historic perspective in Figure 9 where it is compared to previous measurements are referenced in the figure. The energy region of this measurement nicely fills the energy gap between the measurements by fixed-target experiments and previous results from the HERA collaborations.

Acknowledgements

References

[1] I. Abt *et al.* [H1 Collaboration], Nucl. Instrum. Meth. A **386** (1997) 348. doi:10.1016/S0168-9002(96)00894-7

I. Abt *et al.* [H1 Collaboration], Nucl. Instrum. Meth. A **386** (1997) 310. doi:10.1016/S0168-9002(96)00893-5

[2] B. List and A. Mastroberardino DESY-PROC-1999-02 (1999) 396

[3] V. M. Budnev, I. F. Ginzburg, G. V. Meledin and V. G. Serbo, Phys. Rept. **15** (1975) 181. doi:10.1016/0370-1573(75)90009-5
C. F. von Weizsacker, Z. Phys. **88** (1934) 612. doi:10.1007/BF01333110
E. J. Williams, Phys. Rev. **45** (1934) 729. doi:10.1103/PhysRev.45.729

[4] J. J. Sakurai, Phys. Rev. Lett. **22** (1969) 981. doi:10.1103/PhysRevLett.22.981

[5] S. Aid *et al.* [H1 Collaboration], Nucl. Phys. B **463** (1996) 3 doi:10.1016/0550-3213(96)00045-4 [hep-ex/9601004].

[6] J. Breitweg *et al.* [ZEUS Collaboration], Eur. Phys. J. C **2** (1998) 247 doi:10.1007/s100520050136 [hep-ex/9712020].

[7] M. Derrick *et al.* [ZEUS Collaboration], Z. Phys. C **69** (1995) 39 doi:10.1007/s002880050004 [hep-ex/9507011].

[8] S. Schmitt, JINST **7** (2012) T10003 doi:10.1088/1748-0221/7/10/T10003 [arXiv:1205.6201 [physics.data-an]].

[9] H. Abramowicz *et al.* [ZEUS Collaboration], Eur. Phys. J. C **72** (2012) 1869 doi:10.1140/epjc/s10052-012-1869-5 [arXiv:1111.4905 [hep-ex]].

[10] T. Sjostrand, hep-ph/9508391.

[11] E. Fermi, Z. Phys. **29** (1924) 315. doi:10.1007/BF03184853

[12] E. J. Williams, Phys. Rev. **45** (1934) 729. doi:10.1103/PhysRev.45.729

[13] C. F. von Weizsacker, Z. Phys. **88** (1934) 612. doi:10.1007/BF01333110

[14] V. M. Budnev, I. F. Ginzburg, G. V. Meledin and V. G. Serbo, Phys. Rept. **15** (1975) 181. doi:10.1016/0370-1573(75)90009-5

[15] J. J. Sakurai, Phys. Rev. Lett. **22** (1969) 981. doi:10.1103/PhysRevLett.22.981

[16] J. J. Sakurai and D. Schildknecht, Phys. Lett. **40B** (1972) 121. doi:10.1016/0370-2693(72)90300-0

[17] J. J. Sakurai and D. Schildknecht, Phys. Lett. **41B** (1972) 489. doi:10.1016/0370-2693(72)90682-X

[18] J. J. Sakurai and D. Schildknecht, Phys. Lett. **42B** (1972) 216. doi:10.1016/0370-2693(72)90065-2

[19] T. H. Bauer, R. D. Spital, D. R. Yennie and F. M. Pipkin, Rev. Mod. Phys. **50** (1978) 261 Erratum: [Rev. Mod. Phys. **51** (1979) 407]. doi:10.1103/RevModPhys.50.261

[20] G. F. Chew and S. C. Frautschi, Phys. Rev. Lett. **8** (1962) 41. doi:10.1103/PhysRevLett.8.41

[21] V. N. Gribov, Sov. Phys. JETP **14** (1962) 1395 [Zh. Eksp. Teor. Fiz. **41** (1961) 1962].

[22] C. Lovelace, Nuovo Cim **25** (1962) 730. doi:https://doi.org/10.1007/BF02733144

[23] Y. Akimov *et al.*, Phys. Rev. D **14** (1976) 3148. doi:10.1103/PhysRevD.14.3148

[24] K. A. Goulianos, Phys. Rept. **101** (1983) 169. doi:10.1016/0370-1573(83)90010-8

[25] M. Tanabashi *et al.* (Particle Data Group), Phys. Rev. D **98** (2018) 030001.

[26] S. M. Wang [H1 and ZEUS Collaborations], AIP Conf. Proc. **412** (1997) no.1, 599. doi:10.1063/1.54263

[27] J. Breitweg *et al.* [ZEUS Collaboration], Eur. Phys. J. C **14** (2000) 213 doi:10.1007/s100520000374 [hep-ex/9910038].

[28] P. Soding, Phys. Lett. **19** (1966) 702. doi:10.1016/0031-9163(66)90451-3

[29] G. Breit and E. Wigner, Phys. Rev. **49** (1936) 519. doi:10.1103/PhysRev.49.519

[30] R. Brun, F. Bruyant, F. Carminati, S. Giani, M. Maire, A. McPherson, G. Patrick and L. Urban, doi:10.17181/CERN.MUHF.DMJ1

14
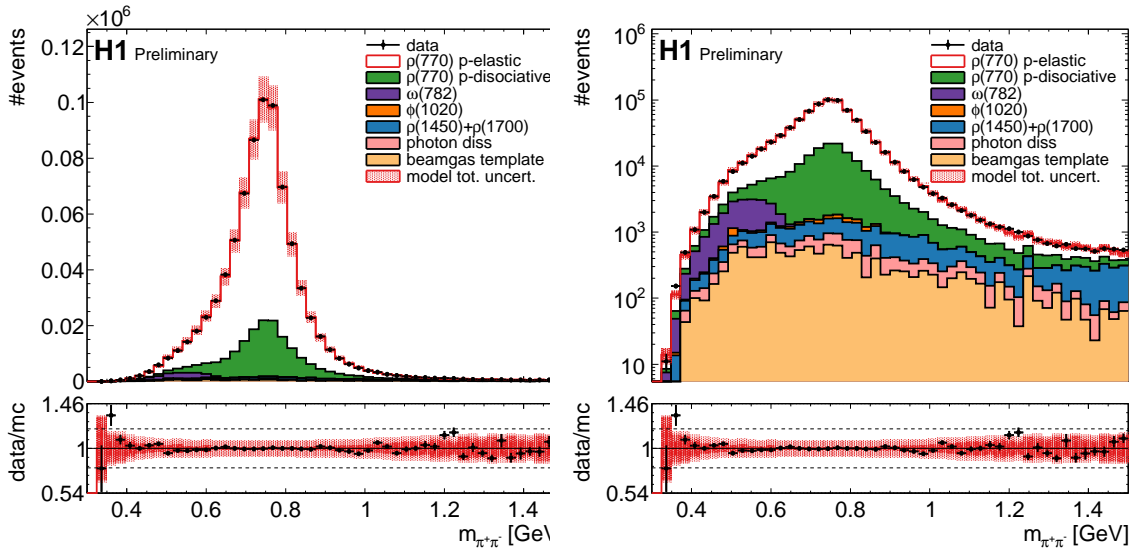
Figure 2: Invariant $\pi^+\pi^-$ mass distribution of selected events in the signal region in comparison to the tuned model prediction on a linear (left) and logarithmic y-scale (right).
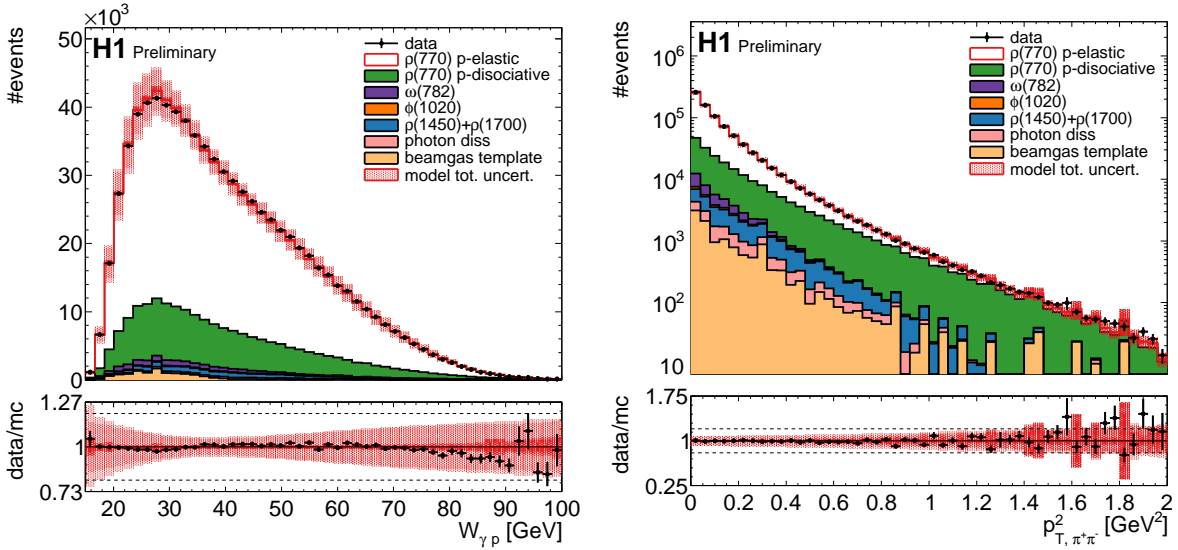
Figure 3: $W_{\gamma p}$ (left) and $p^2_{T,\pi^+\pi^-}$ (right) distribution of selected events in the signal region in comparison to the tuned model prediction.
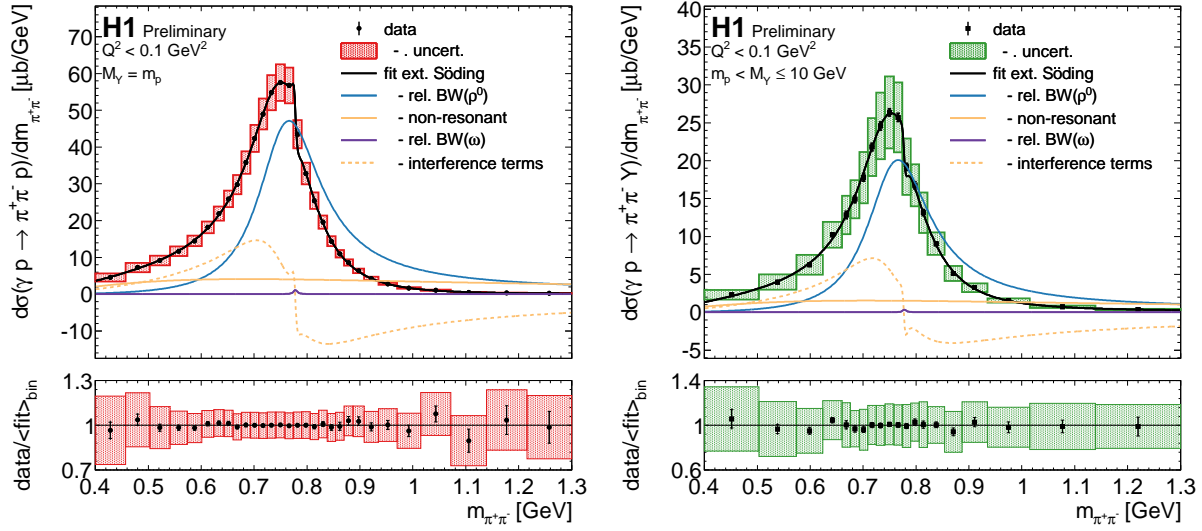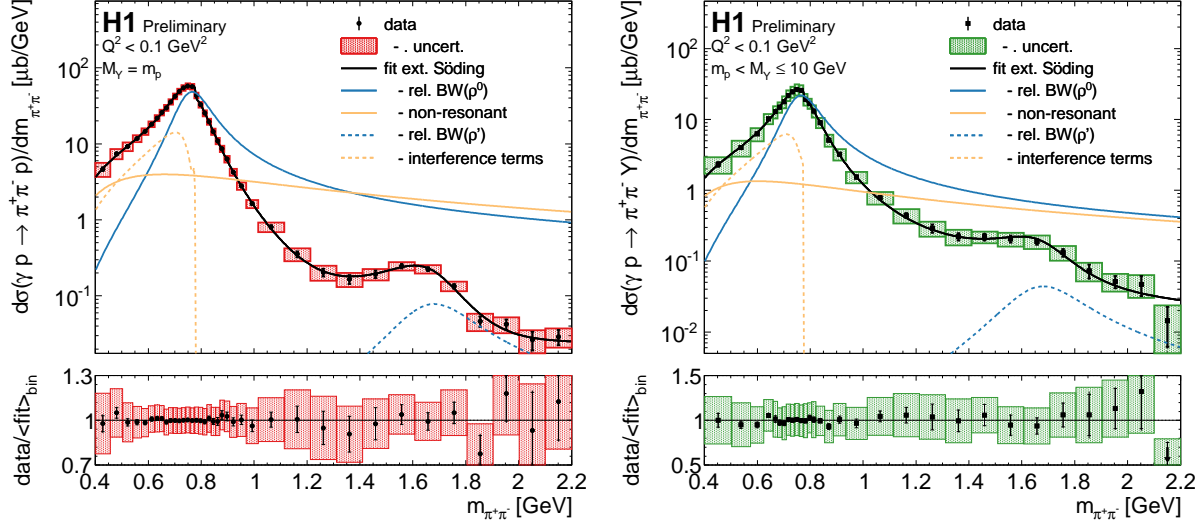
Figure 4: Differential cross-section $d\sigma(\gamma p \to \pi^+\pi^- X)/dm_{\pi^+\pi^-}$ as a function of $m_{\pi^+\pi^-}$ for elastic (left) and proton-dissociative events (right). The data points in black are shown together with statistical uncertainties from data and due to the limited size of the MC samples used for the unfolding. The size of the data uncertainties alone is indicated by the horizontal lines on the error markers. The two distributions are simultaneously fitted using the parametrization given in Equation (10) and fit function is shown together with a subset of contributing components.
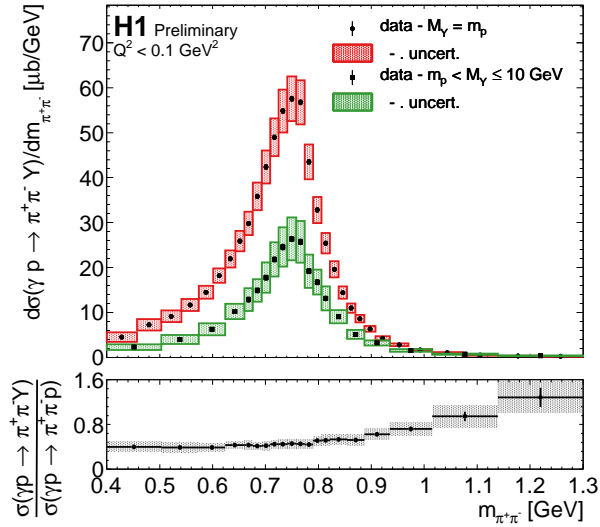
Figure 5: Comparison of the elastic and proton-dissociative differential cross-section $d\sigma(\gamma p \to \pi^+\pi^- X)/dm_{\pi^+\pi^-}$ as a function of $m_{\pi^+\pi^-}$. The composition of the data errors is explained in Figure 4.

16

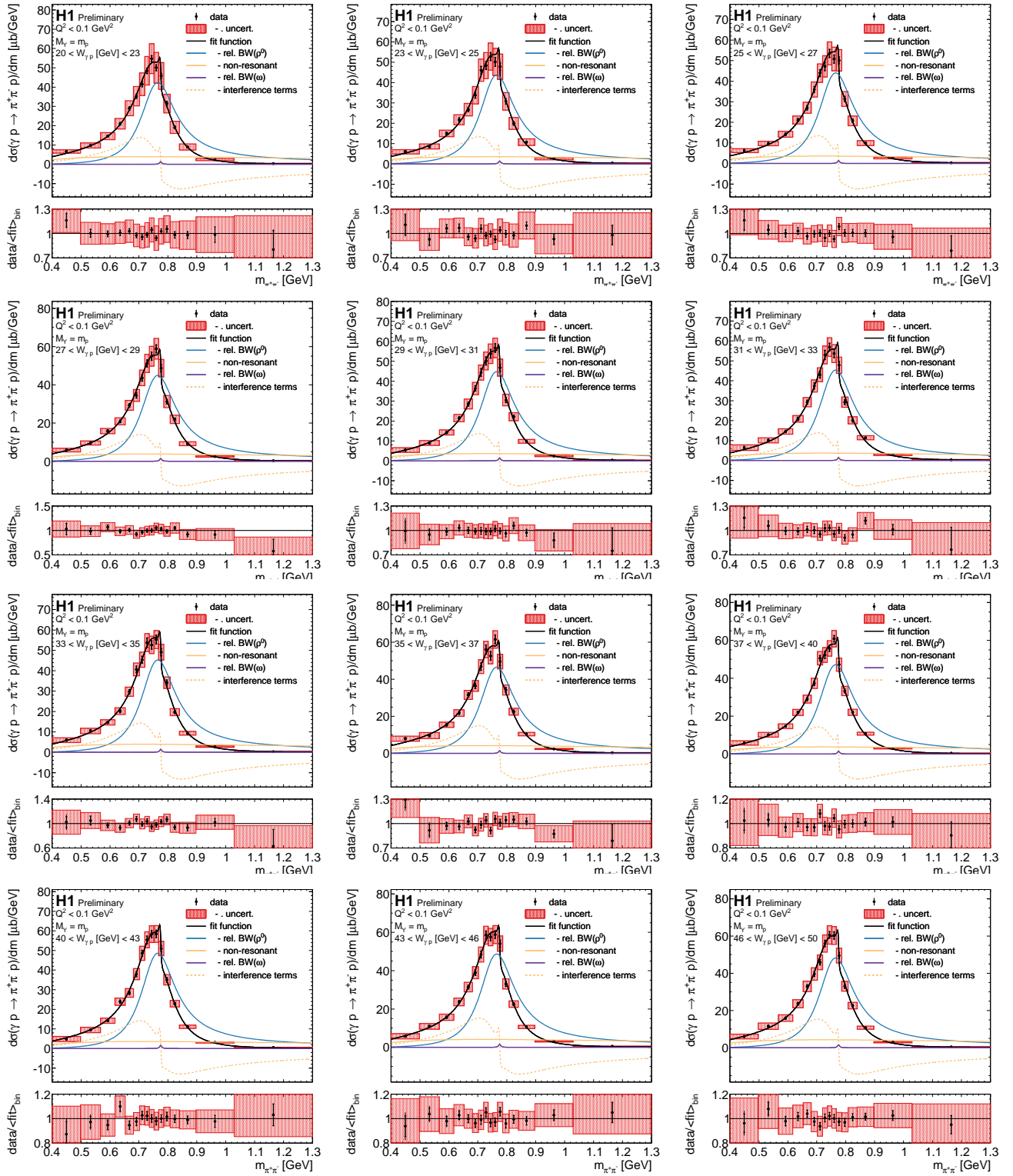Figure 6: Differential cross-section $\mathrm{d}\sigma(\gamma p \to \pi^+\pi^- X)/\mathrm{d}m_{\pi^+\pi^-}$ as a function of $m_{\pi^+\pi^-}$ for elastic (left) and proton-dissociative events (right) with the mass range extended to 2 GeV. Between $1.4 \lesssim m_{\pi^+\pi^-} \lesssim 1.8$ a second large resonance can be observed. The two distributions are simultaneously fitted using the parametrization given in Equation (10) extended by second Breit-Wigner resonance in analogy to the ω contribution. The fit function is shown together with a subset of contributing components. The composition of the data errors is explained in Figure 4.

Table 4: Fiducial elastic and proton-dissociative $\pi^+\pi^-$ photoproduction cross-sections obtained from unfolding the $m_{\pi^+\pi^-}$ distribution in the phasespace defined in Table 2. Systematic uncertainties not fully evaluated.

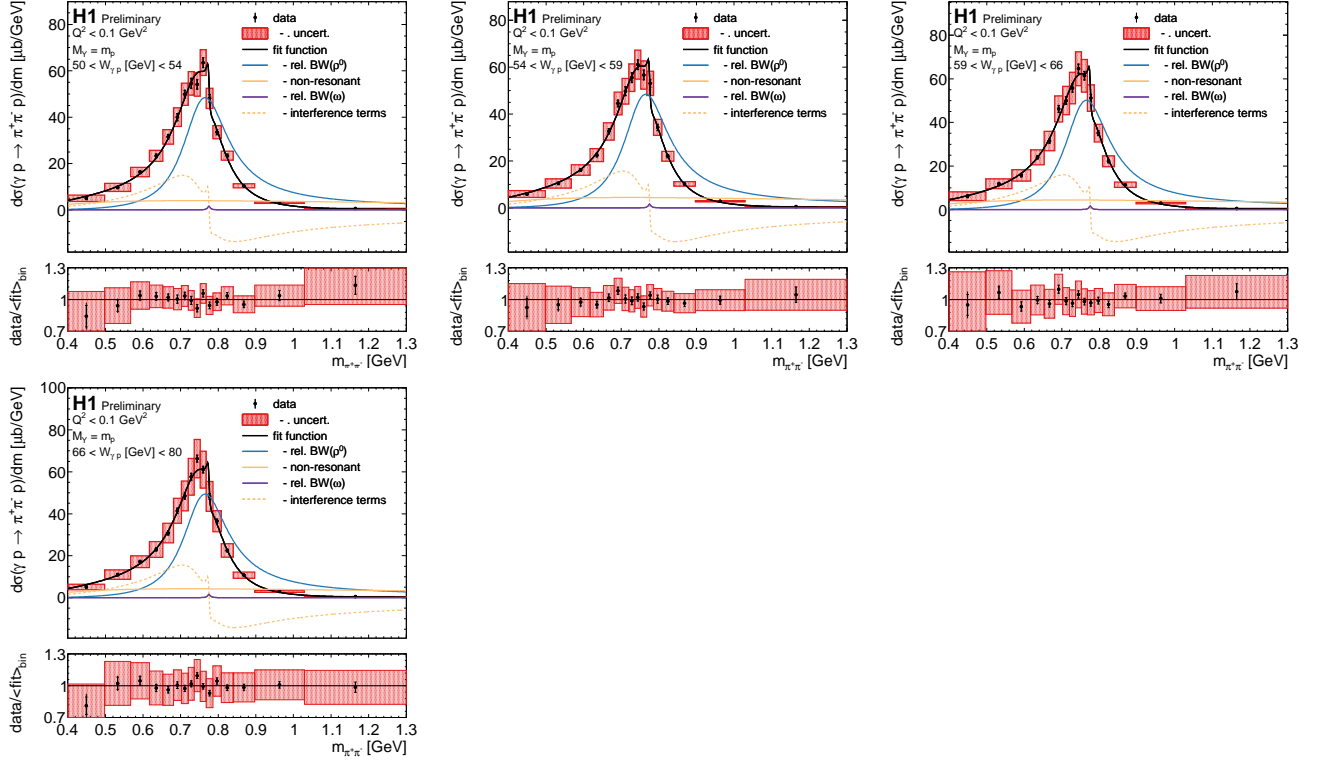| $\sigma\,[\mu\mathrm{b}]$	stat.$\,[\mu\mathrm{b}]$	syst. $[\mu\mathrm{b}]$ (%)
elastic		
11.36	0.05	1.03 (9.0)
p-dissociative		
6.22	0.06	1.14 (18.3)

17

Multi-page figure; for caption see Figure 6

Figure 6: Elastic differential cross-section $\mathrm{d}\sigma(\gamma p \to \pi^+\pi^- p)/\mathrm{d}m_{\pi^+\pi^-}$ as a function of $m_{\pi^+\pi^-}$ shown in 16 bins of rising $W_{\gamma p}$ (from left to right, top to bottom). The elastic distributions are simultaneously fitted together with the proton-dissociative distributions shown in Figure 7 using the parametrization given in Equation (10). The fit function for the respective bins is shown together with a subset of contributing components. The composition of the data errors is explained in Figure 4.
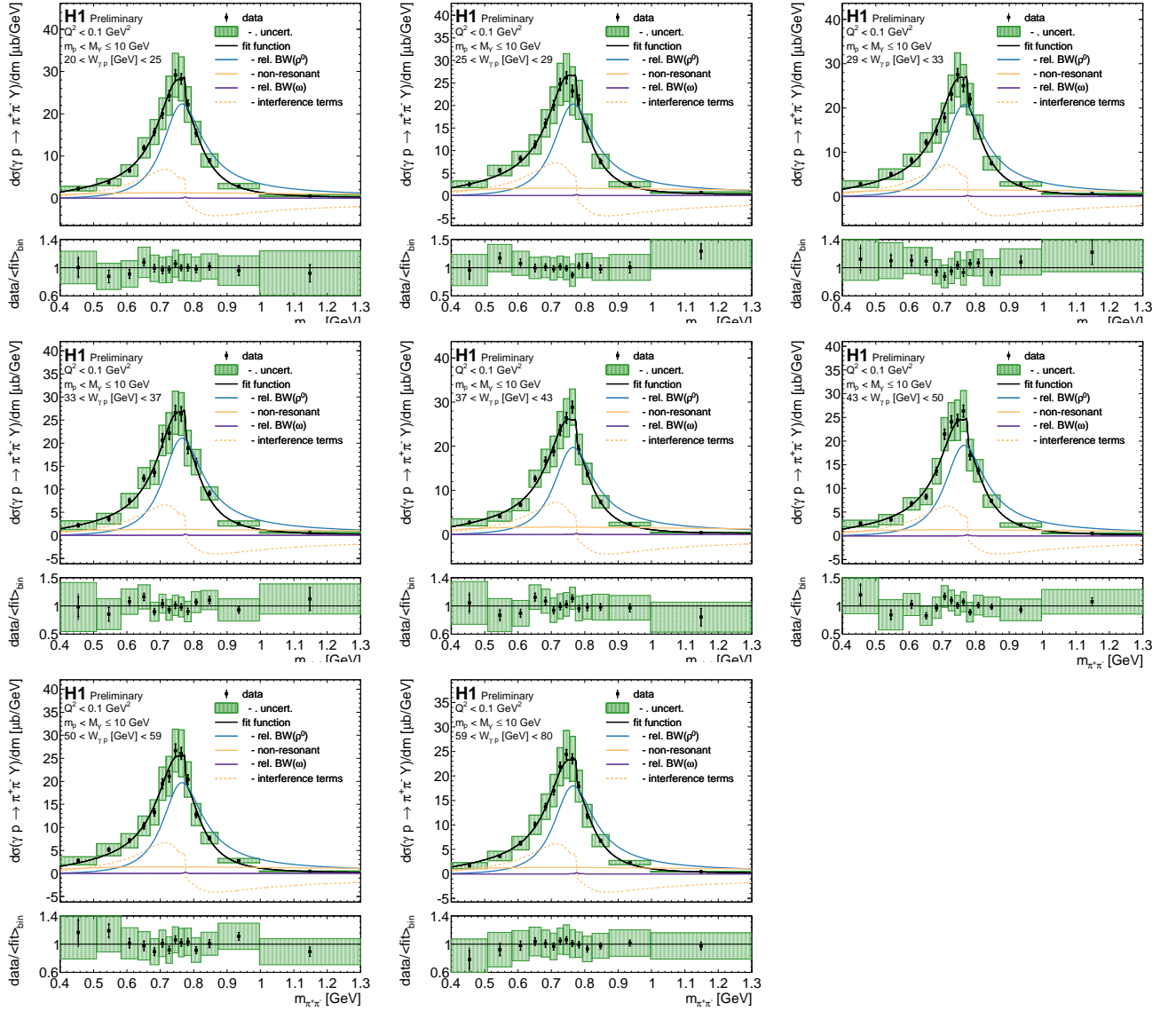
Figure 7: proton-dissociative differential cross-section $d\sigma(\gamma p \to \pi^+\pi^- X)/dm_{\pi^+\pi^-}$ as a function of $m_{\pi^+\pi^-}$ shown in 8 bins of rising $W_{\gamma p}$ (from left to right, top to bottom). The elastic distributions are simultaneously fitted together with the proton-dissociative distributions shown in Figure 6 using the parametrization given in Equation (10). The fit function for the respective bins is shown together with a subset of contributing components. The composition of the data errors is explained in Figure 4.
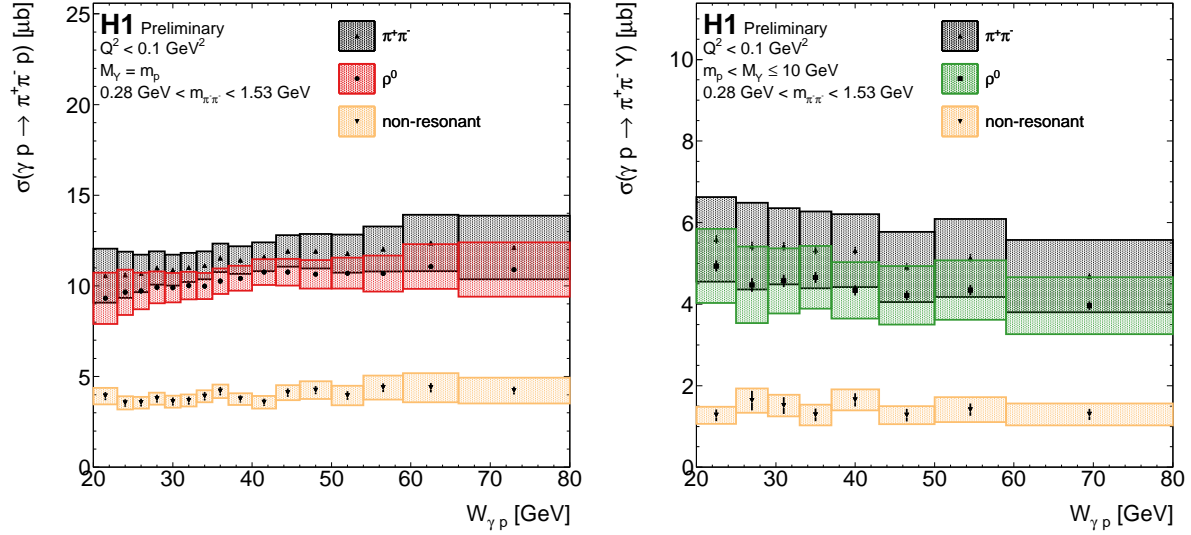
Figure 8: Contributions from ρ^0 and non-resonant production to the total cross-section $\sigma(\gamma p \to \pi^+\pi^- X)$ for elastic (left) and proton-dissociative events (right) as a function of $W_{\gamma p}$. The contributions are obtained by integrating the respective components to the fit-functions shown in Figures 6 and 7 over the range $2m_\pi < m_{\pi^+\pi^-} < 1.53$ GeV. The shown total and statistical uncertainties are obtained by propagating the fit parameter uncertainties through the integration. The composition of the data errors is explained in Figure 4.
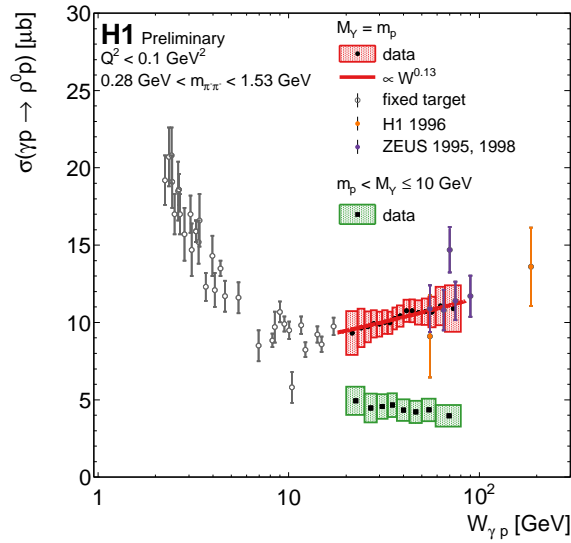

Figure 9: Comparison of the total cross-section $\sigma(\gamma p \to \rho^0 X)$ for elastic and proton-dissociative events as a function of $W_{\gamma p}$. For illustration, high energy data for $\sigma(\gamma p \to \rho^0 p)$ from H1 [5] and ZEUS [6,7] at HERA as well as data from fixed target experiments, as referenced in [6], are included. The composition of the data errors is explained in Figure 4.

21